DOI: 10.1039/c9cp05717j

PCCP

PAPER

View Article Online
View Journal | View Issue

Check for updates

Cite this: *Phys. Chem. Chem. Phys.*, 2020, **22**, 5839

Received 21st October 2019,
Accepted 17th February 2020

DOI: 10.1039/c9cp05717j

rsc.li/pccp

Deterministic control of surface mounted metal–organic framework growth orientation on metallic and insulating surfaces†

Tatiana Parra Vello,[ab] Mathias Strauss,[a] Carlos Alberto Rodrigues Costa,[a]
Cátia Crispilho Corrêa[a] and Carlos César Bof Bufon *[abc]

Surface-Mounted Metal–Organic Frameworks (SURMOFs) are promising materials with a wide range of applications and increasing interest in different technological fields. The use of SURMOFs as both the active and passive tail in electronic devices is one of the most exciting possibilities for such a hybrid material. In such a context, the adhesion, roughness, and crystallinity control of SURMOF thin films are challenging and have limited their application in new functional electronic devices. Self-assembled monolayers (SAMs), which ensure the effective attachment of the SURMOF onto substrates, also play a critical role that can profoundly affect the SURMOF growth mechanism. Herein, we demonstrate that the deterministic control of the SAM chain length influences the preferential orientation of SURMOF films. As the SAM chain length increases, HKUST-1 thin films tend to change their preferential orientation from the [111] towards the [100] direction. Such control can be achieved on both electrically conducting and insulating substrates, opening the possibility of having the very same preferential crystalline orientation on surfaces of different nature, which is of fundamental importance for SURMOF-based functional electronic devices.

Introduction

Metal–organic frameworks (MOFs) are hybrid porous materials formed by assembling organic linkers and metal/metal-oxo nodes *via* coordination bonds. The combination of high crystallinity and porosity has highlighted MOFs as relevant materials for gas storage and catalysis, as well as membranes for molecule separation. The variety of possible structural geometries associated with chemical tailorability has broadened the application range of these materials to technological fields such as chemical and biological sensors,[1–4] energy storage,[5–7] solid-state components,[8–10] and electronic/photoelectronic devices,[11–15] to mention a few. Notably, the application of MOF thin films in electronic devices has gained attention in recent years.[16,17] Also, the thermal and chemical stability of several MOFs allow their integration into microfabrication processes.[16] The tunable framework and the possibility of filling their pores with functional guest molecules have further improved the control of MOFs' electronic properties.[8] Such features are of relevance and enable device engineering rules that can select a particular MOF for a specific application.

Despite all those advantages, the use of MOFs in electronics still represents a challenge. A device's overall physical and chemical properties are strongly dependent on the interaction between the host surfaces (*e.g.*, the metallic contacts and insulating surfaces) and the functional material. Although several deposition methods for MOF powder have been reported, effective integration into devices requires, very often, rigorous control of key figures-of-merit, including the surface roughness, crystalline orientation, and thickness of the deposited films.[16,18]

The layer-by-layer (LbL) approach to synthesize Surface-mounted Metal–Organic Frameworks (SURMOFs) is nowadays an effective way to incorporate homogenous thin films of such functional materials onto the device's surface.[19,20] SURMOF growth can occur on top of surfaces previously functionalized by self-assembled monolayers (SAMs), having an organic group tail (*e.g.*, –COOH, –OH), which mimic the organic ligand's groups, allowing the attachment of the first layer of the ionic cluster on the surface. The use of SAMs as an anchor to grow SURMOF films has been successfully applied to metallic surfaces to ensure well-attached and low-roughness films.[21]

The SURMOF growth mechanism strongly depends on the synthesis temperature,[22,23] reactant solvent medium,[24,25] and

---

[a] *Brazilian Nanotechnology National Laboratory (LNNano), Brazilian Center for Research in Energy and Materials (CNPEM), Zip Code 13083-970, Campinas, Sao Paulo, Brazil. E-mail: cesar.bof@Lnnano.cnpem.br*

[b] *Department of Physical Chemistry, Institute of Chemistry (IQ), UNICAMP, 13084-862, Campinas, SP, Brazil*

[c] *Postgraduate Program in Materials Science and Technology (POSMAT), São Paulo State University (UNESP), 17033-360 Bauru, SP, Brazil*

† Electronic supplementary information (ESI) available. See DOI: 10.1039/c9cp05717j

time of exposure to the reactant solutions,[26] to mention a few. These parameters are responsible for modifying the SURMOF crystallinity, film roughness, and preferential growth orientation.

Apart from anchoring MOFs to surfaces, the SAM's functional tail group can also influence the films' crystalline orientation.[27,28] For instance, Biemmi *et al.* used HKUST-1 (derived from Hong Kong University of Science and Technology) to demonstrate that the film orientation could be tuned from the [100] to the [111] direction by substituting –COOH for –OH terminated SAMs. Such tunability evidences the direct influence of the coordination geometry of the SAM tail group with an ionic cluster on the SURMOF growth orientation.[27] Another example of SURMOF orientation control is the use of SAMs with different density packing to align the films towards specific growth orientations.[29]

Herein, we explore for the first time the use of the SAM chain length for controlling the preferential growth orientation of SURMOF films. Considering the importance of the SAM chain length to the electrical properties of hybrid devices and sensors, such as suppressing leakage currents, and enhancing charge carrier mobility and charge injection,[30–32] this study leads to a fundamental understanding of the relationship between the SAM chain length and packing, and the SURMOF texturing. While several studies applying SURMOFs on Au/SAM substrates have been reported, fewer efforts were spent on the study of SURMOFs on insulating surfaces. Towards novel MOF-based functional structures and devices, apart from using conducting substrates, the need for well-controlled crystalline orientation and surface roughness of such hybrid thin films on insulating surfaces is an essential step. Recent reports have evidenced differences in the electrical responses of polycrystalline and oriented SURMOF films.[33,34] Here we propose and demonstrate the use of phosphonic acid SAMs as an anchor to grow HKUST-1 onto oxide films. The growth of HKUST-1 on insulating surfaces (Al_2O_3 for instance), without functionalization by a SAM, has produced films oriented to the [111] direction.[28] This orientation differs from the [100] orientation typically found on conducting surfaces such as Au functionalized with –COOH terminated SAMs.

Therefore, considering a heterogeneous surface present in typical device structures, which comprises metal contacts bridged by insulating layers (typically found on field-effect transistors, for instance), one should expect distinct crystalline orientation for the very same deposited MOF layer. By incorporating the SAM on both metal and oxide layers, we ensure that the preferential growth direction (here [100]) can be deterministically controlled regardless of the surface nature (metallic or insulating). Such an approach further guarantees that SURMOF layers have the very same crystalline structure over heterogeneous surfaces, which is relevant towards SURMOF based hybrid electronics.

Materials and methods

Substrate fabrication

Growth and preferential orientation HKUST-1 SURMOF studies were carried out using 9 × 9 mm $Si/SiO_2(100)$ substrates covered by Cr/Au or Cr/Ni (5 nm/10 nm) films. Cr was used as an adhesion layer, and all metals were deposited by electron-beam evaporation at a 0.5 Å s^{-1} rate. An Al_2O_3 film (15 nm) was deposited onto the Cr/Ni surfaces using the thermal atomic layer deposition (ALD) technique at 150 °C. The deposition process consisted of alternating pulses of trimethylaluminum and water in a reaction chamber (Oxford Opala system).[35,36]

Self-assembled monolayer immobilization and SURMOF deposition

SURMOF films were grown by LbL, which consisted of sequential and alternate dipping of the samples in solutions of individual reactants. Firstly, Au substrate surfaces were modified with one of the four types of SAMs with different length, namely, 3-mercaptopropionic acid (SH-C3) 99%, 6-mercaptohexanoic acid (SH-C6) 90%, 11-mercaptoundecanoic acid (SH-C11) 95%, and 16-mercaptohexadecanoic acid (SH-C16) 90%, purchased from Sigma Aldrich. The SAM immobilization was carried out by immersing the substrate in 0.5 mM SAM prepared in ethanol (99.99% purity)/10% acetic acid solution (99.7% purity).[37] To ensure a reproducible immobilization process, all substrates were initially left in the solution for 1 h at 50 °C, and then additional 19 h at room temperature.[38] Next, the functionalized surfaces underwent the SURMOF deposition cycles by LbL. Each growth cycle comprised 4 immersion steps: (a) 1 mM ethanolic copper acetate (Cu-Ac) solution for 30 min, (b) washing in ethanol, (c) 1 mM ethanolic trimesic acid (BTC) solution for 1 h, and (d) final washing in ethanol. Samples with 5, 10, 20, 30, and 40 cycles were prepared. The very same SURMOF growth protocol was applied to Al_2O_3 surfaces. The difference lies in the initial surface functionalization that relies on phosphonic acid SAMs with different chain lengths: 3-phosphonopropionic acid (PO-C3) 94%, 6-phosphonohexanoic acid (PO-C6) 97%, 11-phosphonoundecanoic acid (PO-C11) 96% and 16-phosphonohexadecanoic acid (PO-C16) 97%. The Al_2O_3 surface modification with phosphonic acid SAMs was performed in propanol (99.5% purity)/5% acetic acid solution.[35,39]

Characterization techniques

X-ray diffractograms (XRD) were measured using the 2-theta configuration in a synchrotron radiation beamline (XRD2-LNLS, Brazil). An incident wavelength of 1.54979 Å and a Mythen linear detector were used for data acquisition. Diffractograms were acquired between 5 and 20° (2θ). Scanning electron microscopy (SEM) images were obtained using an FEI Inspect F50 microscope with an Everhart Thornley secondary electron detector and samples were previously coated with carbon film deposited by a sputtering technique. Atomic force microscopy (AFM) images (512 × 512 pixels) were obtained with a Park Systems NX10 microscope with an NX-AFM controller, operating in peak force tapping mode, and using a silicon tip coated with Al, from NanoWorld. The AFM tips used here have a nominal resonant frequency of 75 kHz and a nominal force constant of 2.8 N m^{-1}. X-ray photoelectron spectra (XPS) were acquired using a Thermo Scientific Kα micro-focused monochromatized source with a resolution of 0.1 eV, a pass energy of 50 eV with a spot size of 300 μm and 20 scans. 3D laser scanning confocal microscopy

(LSCM) was performed using a Keyence model VK-X200 series, Osaka, Japan. The electrochemical measurements used a three-electrode cell connected to a potentiostat/galvanostat (AutoLab PGSTAT302N with FRA mode, Methrom).

Results and discussion

Fig. 1a shows X-ray diffractograms for a series of HKUST-1 films (40 cycles) deposited on Au surfaces with and without SAMs of

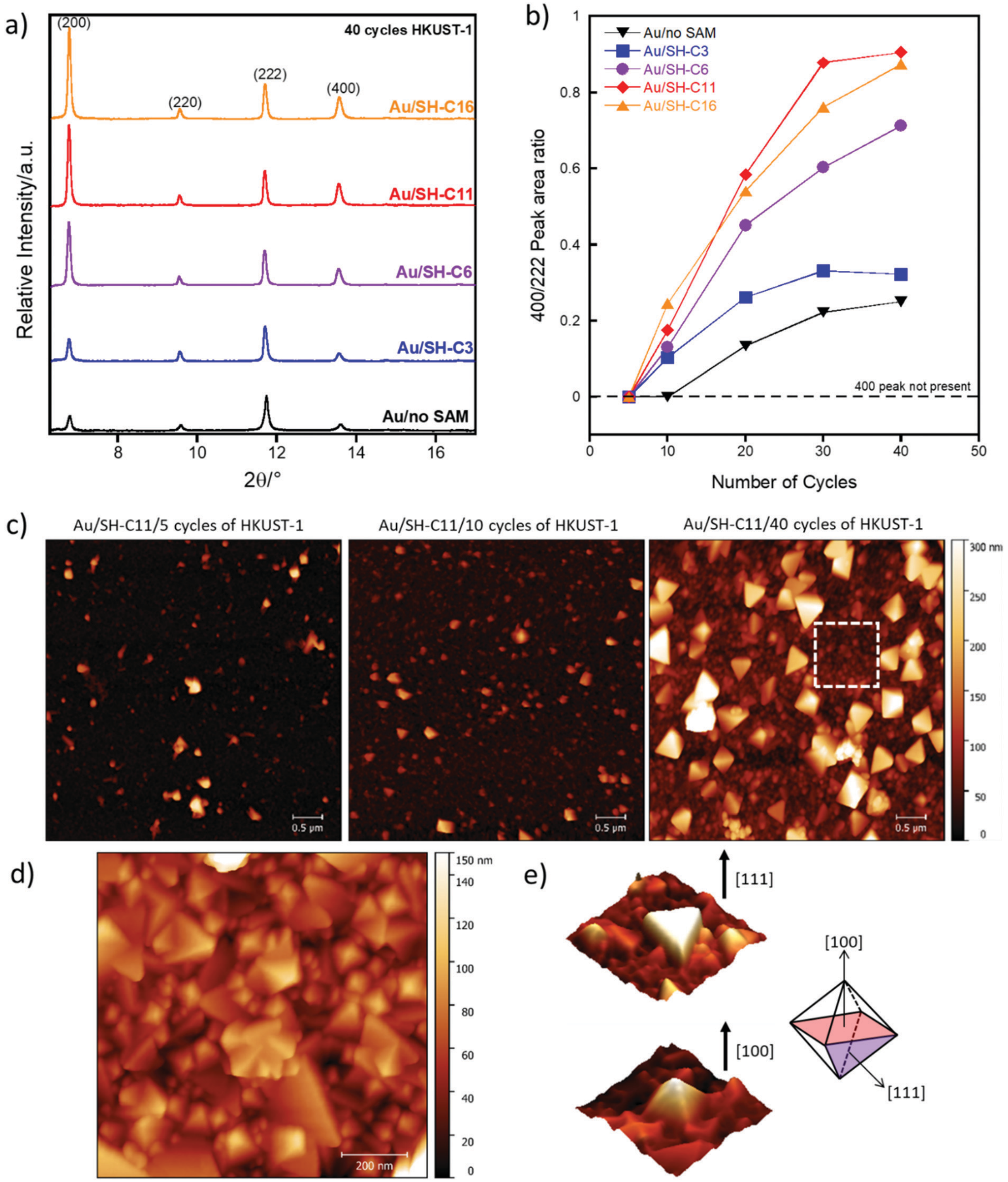

Fig. 1 (a) X-ray diffractograms for the 40-cycle HKUST-1 films grown on bare Au and Au surfaces functionalized with thiolated SAMs of different chain lengths (comprising 3, 6, 11, and 16 carbons). Their respective 222 peak intensity value is normalized for all diffractograms. (b) Area ratio of the 400 and 222 peaks as a function of the number of deposition cycles. The comparison between the peaks is made for both bare Au and SAM functionalized surfaces. The 400 peak was chosen instead of the 200 peak to avoid the background signal present at low angles, which can suppress the [200] peak for thinner films. (c) 5 × 5 μm AFM images of Au/SH-C11 samples with 5, 10, and 40 cycles of HKUST-1. (d) 1 × 1 μm AFM image of Au/SH-C11/40 cycles of HKUST-1 corresponding to regions of smaller crystals as highlighted in (c). (e) Examples of [111] (triangular) and [100] (pyramidal) crystals.

different chain lengths. In all cases, the HKUST-1 film was formed on the respective surfaces. Fig. S1 (ESI†) shows the SEM images of a 20-cycle HKUST-1 film grown on a bare Au surface, and on top of a Au/SH-C6 functional layer. It is clear from the image that, apart from the crystalline orientation, the HKUST-1 surface coverage is also modified by surface functionalization, creating a more homogenous film when the SAM is used. In this case, the root-mean-square (rms) surface roughness changes from 230 ± 40 nm to 83 ± 5 nm for HKUST-1 on bare Au and Au/SH-C6 surfaces, respectively (Fig. S2, ESI†). Furthermore, the film adhesion to bare Au is weaker when compared to the Au-functionalized surface (Fig. S2, ESI†), as film delamination is seen.

Comparing the peak intensities (Fig. 1a), we observe that the preferential orientation of the HKUST-1 film changes from the [111] to the [100] direction as the SAM chain length gradually increases. Although the SAMs with COOH terminal groups push HKUST-1 crystallites to grow towards the [100] direction,[27,28] we verified that the SAM termination is not the only relevant figure-of-merit that defines the thin film orientation, since the SAM chain length directly influences the SURMOF growth.

We proceed to evaluate the growth direction of HKUST-1 films as a function of the number of deposition cycles (see Fig. 1b). The area ratio related to the (222) and (400) peaks is used as the primary quantity to evaluate the HKUST-1 growth on bare and SAM-functionalized Au surfaces. Regardless of the surface, there is a clear tendency of orientation towards the [100] direction as the number of growth cycles increases. A similar phenomenon was reported by Nijem *et al.*, where SURMOF films tend to grow in the [100] direction with an increasing number of cycles, regardless of the surface functional group.[40] The dynamics of crystallite growth can be analyzed by the peak full-width half-maximum (FWHM) values. The evolution of the crystallite sizes, for both the (222) and (400) peaks (see Fig. S3, ESI†), is calculated using the Scherrer equation $D = K\lambda/\beta\cos\theta - D$ is the crystal domain size, K the Scherrer constant (= 0.9),[41] θ the diffraction angle, λ the wavelength of the incident radiation, and β the peak width. The calculated average size of islands is in Table S1 (ESI†). Considering the variation of domain sizes from 10 to 40 cycles, the growth rates of [111] and [100] crystallites are 1.1 ± 0.2 and 1.3 ± 0.1 nm per cycle, respectively. The growth rate is similar for both types of crystallites. The difference between [100] and [111] crystallites is evidenced by comparing their respective diffractogram peaks for the first deposition cycles. As shown in Fig. S4 (ESI†), [111] peaks are more intense and sharper than [100], indicating the major formation of [111] crystallites for the first deposited layers. This configuration changes as the film thickness increases. Although the growth rates for triangles and squares are similar, a rising number of nucleated squares is noticed.

The AFM images (shown in Fig. 1c–e) exhibit the surface topography of HKUST-1 films with 5, 10, and 40 cycles, grown on the Au/SH-C11 layer. Note that the number of islands increases as the growth evolves. After 40 cycles, the substrate surface is fully coated by some large pyramidal and triangular crystallites, and smaller pyramidal islands which mostly comprise the film (see the region highlighted in Fig. 1c and the image corresponding to this type of region in Fig. 1d). The same profile is exhibited by samples of the 40-cycle HKUST-1 film deposited on SH-C3, SH-C6, and SH-C16 (see Fig. S5 in the ESI†).

The larger [111]- and [100]-oriented crystallites observed on the surface correspond to those nucleated in the first cycles of the deposition. After each growth cycle, these crystallites increase in size while new ones are formed. The evolution towards sharper [100] peaks, as the number of cycles increases (Fig. S4, ESI†), indicates that the new crystallites (Fig. 1c and d) also suffer the transition from [111] to [100]. Nijem *et al.* demonstrated a rearrangement of the HKUST-1 film orientation from [111] to [100] when increasing the number of deposition cycles (from 20 to 80 cycles), regardless of the functional group of the surface.[40] Our results exhibit the very same tendency but using thinner films. The orientation towards [100], regardless of the nature of the surface, can be related to the energy of crystal surfaces. Umemura *et al.* demonstrate that for octahedral crystallites, the [100] planes show lower energy, and, consequently, more stability than the [111] faces.[42]

The tendency of film orientation towards [100] by changing the number of deposited HKUST-1 layers can also be tuned by specific SAM chain lengths. For shorter chain lengths (SH-C3 on Au), smooth changes in the 400/222 peak area ratio occur as the number of cycles evolves. The use of longer SAMs, SH-C11, and SH-C16, for instance, promotes a more pronounced peak area ratio change. Considering that all SAMs have the same functional group termination, differences among film growth mechanisms can be a direct consequence of the SAM surface coverage driven by the chain length.

The SAMs with long alkane chains are arranged in a densely packed configuration, where the van der Waals interaction keeps the chains aligned. Short-chain SAMs due to their small number of $-CH_2-$ groups tend to be more sparsely packed.[43] Fig. 2a shows the contact-angle measurements carried out on the SAM functionalized Au substrates. As the SAM chain length increases from 3 to 16 carbons the contact angle decreases, indicating a more close-packed monolayer that leads to better aligned –COOH functional groups. This effective alignment is a necessary condition to start the SURMOF growth preferentially oriented to the [100] direction (see the sketch in Fig. 2b). More sparsely-packed SAMs with shorter alkane chains allow alternative crystallographic growth directions as the terminal –COOH groups are not well aligned. The Au surface coverage by SAMs is further supported by cyclic voltammetry and electrochemical impedance spectroscopy obtained in the presence of a $Fe(CN)^{3-/4-}$ redox probe (see Fig. S6 for details, ESI†). As expected, a stronger van der Waals interaction allows better surface coating.

The influence of the SAM surface coverage on the HKUST-1 film growth was also evaluated by XPS. Two sets of samples were prepared by immobilizing SAMs with short (SH-C3) and long (SH-C16) chain lengths on Au surfaces. Afterwards, all surfaces were exposed to Cu-Ac solution for 30 minutes, creating a ''half-cycle'' HKUST-1 film, as illustrated in the scheme of Fig. 2b. The XPS data in Fig. 2c exhibit four characteristic peaks in the carbon spectra: C–C, COOH, C=O and C–O. To elucidate the interactions between Cu-Ac and the SAM's carboxylic tail,

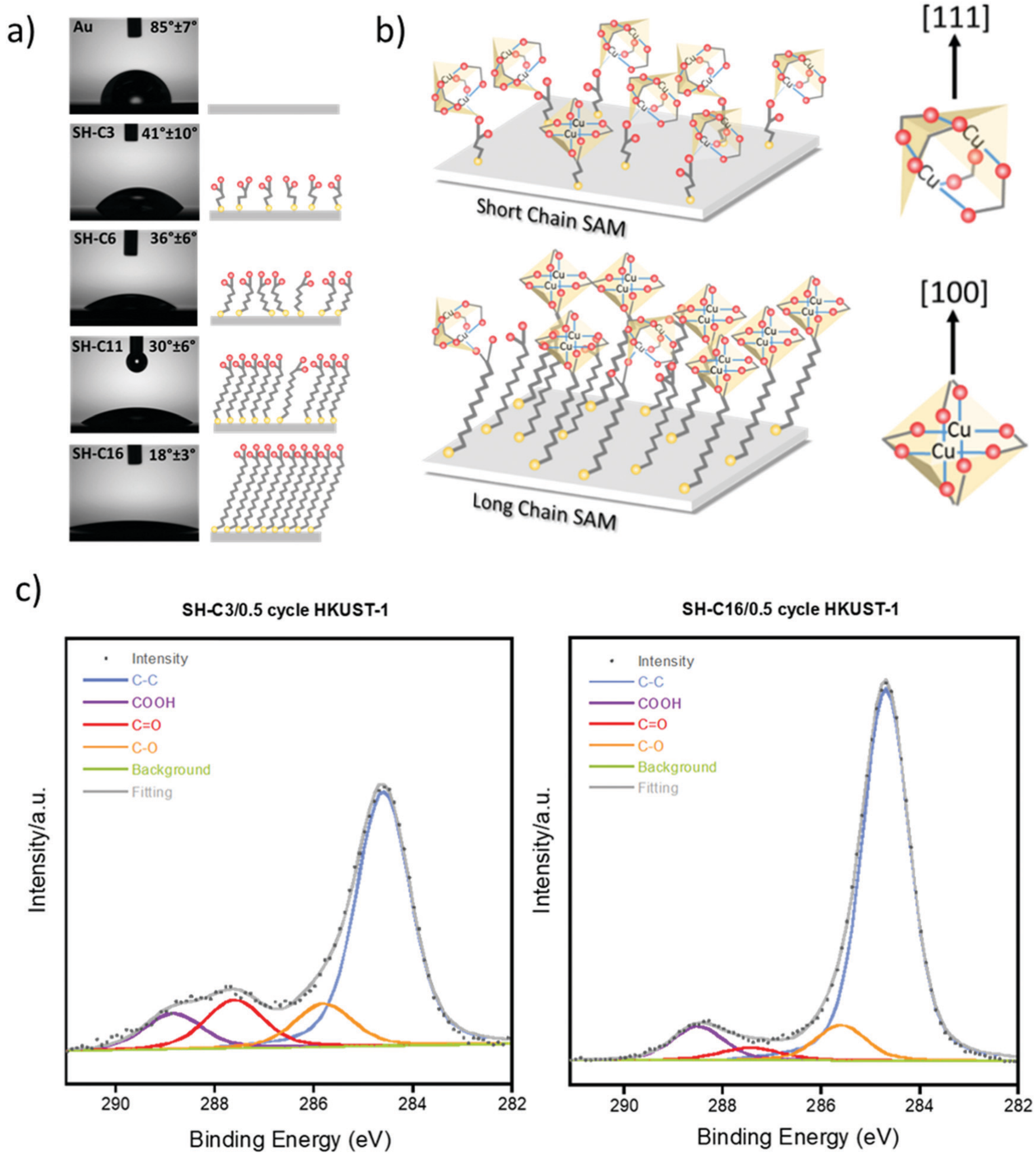

Fig. 2 (a) Contact-angle measurements for SH-C3, SH-C6, SH-C11, and SH-C16 on Au (left). Scheme of SAM packing (right). (b) Scheme of the SAM/Cu-Ac interface. A sparsely-packed short-chain SAM creates a more poorly aligned monolayer, supporting the apical binding of –COOH functional groups and Cu-Ac clusters (a higher number of [111] crystallites). Long-chain SAMs are densely packed, creating an aligned and well-organized layer, which allows paddle-wheel binding between –COOH functional groups and Cu-Ac clusters (a higher number of [100] crystallites). (c) High-resolution carbon XPS spectra for Au/SH-C3 and Au/SH-C16 after immersion only in Cu-Ac solution (0.5 cycles).

we verified that the SH-C3/0.5-cycle sample presents a C=O peak slightly more intense than the COOH and C–O peaks. For the SH-C16/0.5-cycle sample, the COOH and C–O peaks show double the intensity compared to the C=O peak. The COOH and C–O peaks are related to the paddle-wheel bonds, where the carboxylic group of acetate molecules and the carboxylic SAM functional group are linked to both coppers of the metal cluster. The C=O peak arises from the bond between a single oxygen from the SAM's carboxylic group and a copper from the ion cluster. In such a configuration, the non-bonded oxygen from the SAM's carboxylic group remains double-bonded to carbon. The C=O atomic percentage is about three times higher for the SH-C3 immobilized samples (13.4%) than for the SH-C16 ones (3.7%) (Table 1). The data were shown to be reproducible across multiple experiments, as shown in Table S3 (ESI†). The presence of such bonds at the SAM/CuAc interface is also noticed for the oxygen XPS data, where C=O is more intense for SH-C3 than for the SH-C16 system (see Fig. S7 in the ESI†).

The approach to determine the SURMOF growth direction has been previously demonstrated by Biemmi *et al.*[27] The use of

Table 1 XPS binding energy, full width at half maximum (FWHM), and atomic percentage values of carbon species of Au/SH-C3 and Au/SH-C16 with 0.5 cycles of HKUST-1

SAM/0.5 cycle HKUST-1	Peak	Binding energy/eV	FWHM/eV	Atomic abundance/%
SH-C3	C–C	284.6	1.3	64.9
	COOH	288.8	1.4	9.9
	C=O	287.6	1.4	13.4
	C–O	285.8	1.4	11.8
SH-C16	C–C	284.7	1.1	79.9
	COOH	288.5	1.3	8.2
	C=O	287.5	1.5	3.7
	C–O	285.6	1.2	8.2

SAMs with carboxylic and hydroxylic functional tail groups has created films oriented to [100] and [111], respectively.[27,28] Stavila *et al.* have associated the [111] growth direction with the O-bond of the SAM's hydroxylic group to the apical position of the copper cluster. In our work, sparsely-packed SH-C3 creates an ill-aligned monolayer. Therefore, the interactions between the SAM's functional tail and the metallic cluster are not established solely on the paddle-wheel configuration. In this case, the metallic cluster is immobilized on the SAM by a monodentate configuration. This explains the higher amount of C=O species found in Au/SH-C3. A well-organized SH-C16 SAM on the Au surface allows better alignment of carboxylic groups, creating a favorable interface for paddle-wheel bond interactions with copper clusters. Thus, the C=O intensity in XPS spectra is smaller when compared to the SH-C3 system (Fig. 2c). The scheme presented in Fig. 2b illustrates the possible interactions between short- and long-SAMs, and the Cu-Ac molecules. This observation explains the results where longer chain length SAMs induce SURMOF growth towards the [100] direction. Longer chains are responsible for producing more efficient binding towards this growth direction as the paddle-wheel configuration dominates.

As observed in Fig. 1b, the HKUST-1 films exhibit predominant [111]-oriented crystallites for the very first deposited layers. A higher number of [100] oriented crystallites appears as the number of growth cycles increases. The functionalization with long-chain SAMs resulted in more accentuated growth towards the [100] instead of the [111] direction. Combined with the rise in the number of deposition cycles, the long-chain SAMs also create a propitious interface to nucleate and grow [100] crystallites. Therefore, the level of SAM molecule packing on a substrate surface plays a crucial role in the coordination geometry of the SAM/ionic-cluster interface, which is an essential feature to define the SURMOF film orientation.

The same experiments carried out on functionalized metallic surfaces were also done on $\mathrm{Al_2O_3}$ coated surfaces, as shown in Fig. 3a. The direct deposition of HKUST-1 on a bare $\mathrm{Al_2O_3}$ surface has been previously reported[28] and comprises films aligned towards the [111] direction. Si/$\mathrm{SiO_2}$ insulating surface was also previously modified with a silane-based SAM, but the resulting film exhibited sparsely distributed crystals.[44] Therefore, to the best of our knowledge, this work reports for the first

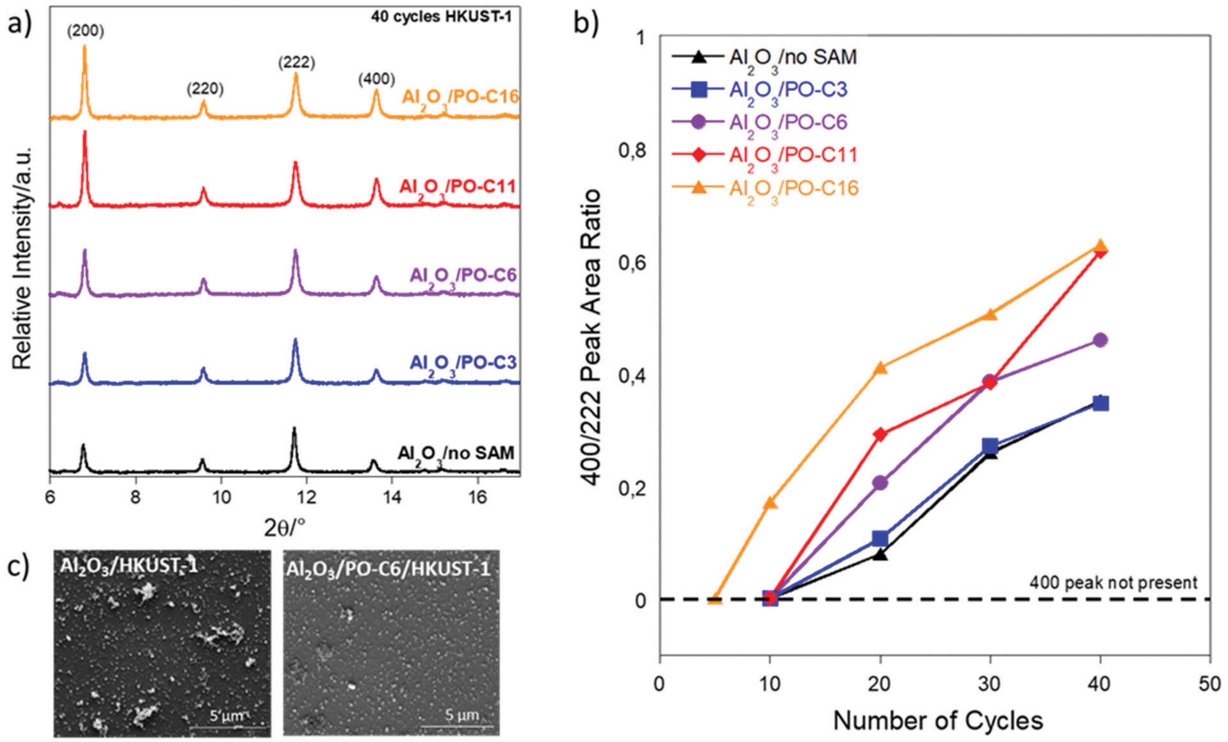

Fig. 3 (a) X-ray diffractograms for 40-cycle HKUST-1 films grown on bare $\mathrm{Al_2O_3}$ and $\mathrm{Al_2O_3}$-functionalized surfaces with phosphonated SAMs (consist of 3, 6, 11 and 16 carbons). All diffractograms were normalized by their respective 222 peak intensity value. (b) Area ratio of 400 and 222 peaks as a function of cycles deposited. A peak comparison is made for bare and functionalized $\mathrm{Al_2O_3}$ surfaces with SAMs of different chain lengths. (c) SEM images of 20-cycle HKUST-1 films grown on bare $\mathrm{Al_2O_3}$ (left), and functionalized $\mathrm{Al_2O_3}$ with SAM PO-C6 (right).

time the use of phosphonic acid SAMs as a functional layer to deterministically control the HKUST-1 growth orientation on an insulating film (Al_2O_3). Similar to what was observed for the Au surfaces, the use of long-chain length SAMs on Al_2O_3 favors the HKUST-1 growth orientation towards the [100] direction as well (see Fig. 3a and b). As shown in Fig. 3c, SURMOF films exhibit homogeneous coating for both bare Al_2O_3 and Al_2O_3/PO-C6 surfaces. In this case, HKUST-1 films grown on bare Al_2O_3 exhibit excellent adhesion to the substrate surface, different from what was observed on the Au surface (morphological information about the Al_2O_3 substrates is shown in Fig. S9 and S10, ESI†). XPS data were acquired for this substrate using the same procedure applied to the Au surface described above. The results also confirm the interaction between the SAM tail group and Cu-acetate cluster (see Fig. S11, ESI†).

By comparing Fig. 1b with Fig. 3b, the HKUST-1 grown on thiol-SAM/Au substrates is better oriented towards the [100] direction than the films grown on phosphonic acid-SAM/Al_2O_3 substrates. The phosphonic acid SAMs present lower packing density when compared to the thiol SAMs.[45,46] Such a difference may influence the chain alignment, leading to better oriented [100] HKUST-1 films on Au than on Al_2O_3. Furthermore, the surface roughness for Al_2O_3 is higher than for the Au-coated surfaces (see Fig. S12, ESI†), which may also influence the SAM immobilization,[47–49] and consequently the orientation of the film.

Regardless of the surface/SAM anchoring group, the chain length determines the preferential growth direction of SURMOFs. Therefore, the immobilization of SAMs on Al_2O_3 surfaces opens the possibility of controlling the orientation of HKUST-1 film growth on insulating materials. Technology-wise, it implies that the SAM chain length can be used as a parameter to control SURMOFs' preferred crystalline orientation on both metallic and insulating substrates. On a heterogeneous substrate, for instance, one could set HKUST-1 to the [111] orientation using short SAMs (*e.g.*, SH-C3 on Au and bare Al_2O_3) or, driven by an application, use longer SAMs (*e.g.*, SH-C16 on Au and PO-C16 on Al_2O_3) to set the SURMOF [100] oriented. Also, considering that in some situations either short or long SAMs are required for the design of electrical devices, the preferential orientation could be predicted and tuned for both metallic and insulating surfaces.

Conclusions

In conclusion, we demonstrated that the preferential orientation of SURMOF films can be set by adjusting the SAM packing, which is controlled by the molecule chain length. The SAM packing on both metallic and insulating surfaces influences the alignment of the carboxylic group tail, favoring equatorial or apical bonding of the SURMOF metallic clusters. The experimental data show that HKUST-1 films change their orientation from the [111] towards the [100] direction on increasing the SAM chain length. Such control can be achieved on both conducting and insulating substrates, opening the possibility of having the very same preferential crystalline orientation on surfaces comprising materials of different nature and electrical properties. To allow immobilization on Au substrates, thiolated SAMs were used, while on Al_2O_3 phosphonic acid SAMs were used. Both surfaces are of fundamental relevance in modern organic and hybrid electronics. To the best of our knowledge, our work offers the first experimental approach to grow homogeneous SURMOF thin films anchored by SAMs on an insulating surface. Regardless of the surface nature, in addition to the control of preferred crystalline orientations, both the surface homogeneity and roughness can be improved by modifying the number of SURMOF deposited layers and the SAM chain length. An impact on electronics, for instance, is expected since the SURMOF layers can have the very same crystalline structure over a heterogeneous surface.

Author contribution

The manuscript was written through the contributions of all authors. All authors have approved the final version of the manuscript.

Abbreviations

SAM	Self-assembled monolayer
SH-C3	3-Mercaptopropionic acid
SH-C6	6-Mercaptohexanoic acid
SH-C11	11-Mercaptoundecanoic acid
SH-C16	16-Mercaptohexadecanoic acid
PO-C3	3-Phosphonopropionic acid
PO-C6	6-Phosphonohexanoic acid
PO-C11	11-Phosphonoundecanoic acid
PO-C16	16-Phosphonohexadecanoic acid
Cu-Ac	Copper-acetate

Conflicts of interest

There are no conflicts to declare.

Acknowledgements

We acknowledge FAPESP (14/25979-2 and 16/25346-5), and CNPq (408770/2018-0) for financial support. C. C. B. B. is a productivity research fellow from CNPq (305305/2016-6). C. C. B. B also acknowledges the support of CNPq and FAPESP (Brazil) through Inomat, National Institute (INCT) for Complex Functional Materials (CNPq Proc 465452/2014-0 and FAPESP 14/50906-9). This research used resources of the Brazilian Synchrotron Light Laboratory (LNLS) and Brazilian Nanotechnology Laboratory (LNNano), open facilities operated by the Brazilian Centre for Research in Energy and Materials (CNPEM). The XRD2 beamline staff is acknowledged for assistance during the experiments (proposal: 20170812 and 20180148). The LNNano research proposals are XPS-24653, SEM-24160, AFM-26354 and AFM-24654. We also thank Emre Yassitepe and Mariane Peres Pereira for fruitful discussions. We also thank the National System of Nanotechnology (SisNANO).

References

1 P. Shi, Y. Zhang, Z. Yu and S. Zhang, *Sci. Rep.*, 2017, **7**, 6500.

2 L. Cui, J. Hu, C. Li, C. Wang and C. Zhang, *Biosens. Bioelectron.*, 2018, **122**, 168–174.

3 M. Campbell and M. Dincă, *Sensors*, 2017, **17**, 1108.

4 D. J. Wales, J. Grand, V. P. Ting, R. D. Burke, K. J. Edler, C. R. Bowen, S. Mintova and A. D. Burrows, *Chem. Soc. Rev.*, 2015, **44**, 4290–4321.

5 L. Wang, X. Feng, L. Ren, Q. Piao, J. Zhong, Y. Wang, H. Li, Y. Chen and B. Wang, *J. Am. Chem. Soc.*, 2015, **137**, 4920–4923.

6 X. Cao, C. Tan, M. Sindoro and H. Zhang, *Chem. Soc. Rev.*, 2017, **46**, 2660–2677.

7 Z. Liang, C. Qu, W. Guo, R. Zou and Q. Xu, *Adv. Mater.*, 2018, **30**, 1702891.

8 A. A. Talin, A. Centrone, A. C. Ford, M. E. Foster, V. Stavila, P. Haney, R. A. Kinney, V. Szalai, F. El Gabaly, H. P. Yoon, F. Leonard and M. D. Allendorf, *Science*, 2014, **343**, 66–69.

9 J. Liu, T. Wächter, A. Irmler, P. G. Weidler, H. Gliemann, F. Pauly, V. Mugnaini, M. Zharnikov and C. Wöll, *ACS Appl. Mater. Interfaces*, 2015, **7**, 9824–9830.

10 M. Usman, S. Mendiratta and K.-L. Lu, *Adv. Mater.*, 2017, **29**, 1605071.

11 Z.-G. Gu, S.-C. Chen, W.-Q. Fu, Q. Zheng and J. Zhang, *ACS Appl. Mater. Interfaces*, 2017, **9**, 7259–7264.

12 G. Wu, J. Huang, Y. Zang, J. He and G. Xu, *J. Am. Chem. Soc.*, 2017, **139**, 1360–1363.

13 M. A. Gordillo, D. K. Panda and S. Saha, *ACS Appl. Mater. Interfaces*, 2019, **11**, 3196–3206.

14 L. Sun, M. G. Campbell and M. Dincă, *Angew. Chem., Int. Ed.*, 2016, **55**, 3566–3579.

15 L. G. S. Albano, T. P. Vello, D. H. S. de Camargo, R. M. L. da Silva, A. C. M. Padilha, A. Fazzio and C. C. B. Bufon, *Nano Lett.*, 2020, **20**, 1080–1088.

16 V. Stavila, A. A. Talin and M. D. Allendorf, *Chem. Soc. Rev.*, 2014, **43**, 5994–6010.

17 M. D. Allendorf, A. Schwartzberg, V. Stavila and A. A. Talin, *Chem. – Eur. J.*, 2011, **17**, 11372–11388.

18 H. Gliemann and C. Wöll, *Mater. Today*, 2012, **15**, 110–116.

19 J. Liu and C. Wöll, *Chem. Soc. Rev.*, 2017, **46**, 5730–5770.

20 L. Heinke and C. Wöll, *Adv. Mater.*, 2019, 1806324.

21 O. Shekhah, H. Wang, S. Kowarik, F. Schreiber, M. Paulus, M. Tolan, C. Sternemann, F. Evers, D. Zacher, R. A. Fischer and C. Wöll, *J. Am. Chem. Soc.*, 2007, **129**, 15118–15119.

22 M. L. Ohnsorg, C. K. Beaudoin and M. E. Anderson, *Langmuir*, 2015, **31**, 6114–6121.

23 J.-L. Zhuang, M. Kind, C. M. Grytz, F. Farr, M. Diefenbach, S. Tussupbayev, M. C. Holthausen and A. Terfort, *J. Am. Chem. Soc.*, 2015, **137**, 8237–8243.

24 R. Khajavian and K. Ghani, *CrystEngComm*, 2018, **20**, 1546–1552.

25 W. Wang, T. Lee and M. A. Reed, *Phys. Rev. B*, 2003, **68**, 035416.

26 G. Delen, Z. Ristanović, L. D. B. Mandemaker and B. M. Weckhuysen, *Chem. – Eur. J.*, 2018, **24**, 187–195.

27 E. Biemmi, C. Scherb and T. Bein, *J. Am. Chem. Soc.*, 2007, **129**, 8054–8055.

28 V. Stavila, J. Volponi, A. M. Katzenmeyer, M. C. Dixon and M. D. Allendorf, *Chem. Sci.*, 2012, **3**, 1531.

29 J. Liu, O. Shekhah, X. Stammer, H. K. Arslan, B. Liu, B. Schüpbach, A. Terfort and C. Wöll, *Materials*, 2012, **5**, 1581–1592.

30 S. Casalini, C. A. Bortolotti, F. Leonardi and F. Biscarini, *Chem. Soc. Rev.*, 2017, **46**, 40–71.

31 P. Stoliar, R. Kshirsagar, M. Massi, P. Annibale, C. Albonetti, D. M. de Leeuw and F. Biscarini, *J. Am. Chem. Soc.*, 2007, **129**, 6477–6484.

32 H. Klauk, U. Zschieschang, J. Pflaum and M. Halik, *Nature*, 2007, **445**, 745–748.

33 X. Chen, Z. Wang, Z. M. Hassan, P. Lin, K. Zhang, H. Baumgart and E. Redel, *ECS J. Solid State Sci. Technol.*, 2017, **6**, P150–P153.

34 X. Chen, Z. Wang, P. Lin, K. Zhang, H. Baumgart, E. Redel and C. Woll, *ECS Trans.*, 2016, **75**, 119–126.

35 T. P. Vello, L. M. B. da Silva, G. O. Silva, D. H. S. de Camargo, C. C. Corrêa and C. C. Bof Bufon, *Biosens. Bioelectron.*, 2017, **87**, 209–215.

36 T. P. Vello, R. F. de Oliveira, G. O. Silva, D. H. S. de Camargo and C. C. B. Bufon, *Sci. Rep.*, 2017, **7**, 43432.

37 R. Arnold, W. Azzam, A. Terfort and C. Wöll, *Langmuir*, 2002, **18**, 3980–3992.

38 C. C. Bof Bufon, J. D. Arias Espinoza, D. J. Thurmer, M. Bauer, C. Deneke, U. Zschieschang, H. Klauk and O. G. Schmidt, *Nano Lett.*, 2011, **11**, 3727–3733.

39 C. C. Bof Bufon, J. D. Cojal González, D. J. Thurmer, D. Grimm, M. Bauer and O. G. Schmidt, *Nano Lett.*, 2010, **10**, 2506–2510.

40 N. Nijem, K. Fürsich, S. T. Kelly, C. Swain, S. R. Leone and M. K. Gilles, *Cryst. Growth Des.*, 2015, **15**, 2948–2957.

41 J. I. Langford and A. J. C. Wilson, *J. Appl. Crystallogr.*, 1978, **11**, 102–113.

42 A. Umemura, S. Diring, S. Furukawa, H. Uehara, T. Tsuruoka and S. Kitagawa, *J. Am. Chem. Soc.*, 2011, **133**, 15506–15513.

43 I. Levine, S. M. Weber, Y. Feldman, T. Bendikov, H. Cohen, D. Cahen and A. Vilan, *Langmuir*, 2012, **28**, 404–415.

44 D. Zacher, A. Baunemann, S. Hermes and R. A. Fischer, *J. Mater. Chem.*, 2007, **17**, 2785.

45 M. Dubey, T. Weidner, L. J. Gamble and D. G. Castner, *Langmuir*, 2010, **26**, 14747–14754.

46 D. M. Spori, N. V. Venkataraman, S. G. P. Tosatti, F. Durmaz, N. D. Spencer and S. Zürcher, *Langmuir*, 2007, **23**, 8053–8060.

47 T. M. Uehara, H. B. de Aguiar, K. Bergamaski and P. B. Miranda, *J. Phys. Chem. C*, 2014, **118**, 20374–20382.

48 S. D. Moré, H. Graaf, M. Baune, C. Wang and T. Urisu, *Jpn. J. Appl. Phys.*, 2002, **41**, 4390–4394.

49 B. G. Bush, F. W. DelRio, J. Opatkiewicz, R. Maboudian and C. Carraro, *J. Phys. Chem. A*, 2007, **111**, 12339–12343.